Robust Heading Measurement Based on Improved Berry Model for Bionic Polarization Navigation

Guangmin Li, Ya Zhang, *Member, IEEE*, Shiwei Fan, Yanyan Wang, and Fei Yu

Abstract—With the advantages of anti-interference and no accumulated error, bionic polarization heading measurement has important military significance and research value for autonomous navigation. However, the heading robustness is seriously affected by the accuracy of the skylight polarization model and the existing methods all use the Rayleigh scattering model without considering atmospheric depolarization. Therefore, this article proposed an innovative method of polarization heading measurement based on the Berry model to consider the influence of depolarization neutral points. And this model is improved by controlling the neutral points with correction coefficients to realize high-robustness heading measurement. On this basis, the improved Berry model is further used to calibrate the sensor parameters outdoors, which separates the skylight polarization model error from the sensor error without expensive instruments and complicated processes and improves the heading measurement accuracy. In the experiments with changing solar altitude, the average heading error STD after field calibration is 20.86% lower than that of the Berry model and 92.85% lower than that of the Rayleigh model, which shows great advancement in actual measurements.

Index Terms—Field calibration, heading measurement, polarization navigation, skylight polarization model.

I. INTRODUCTION

ABSOLUTE heading measurement under the condition of Global Navigation Satellite System (GNSS) rejection or magnetic interference is a challenging problem [1], [2], [3]. However, to meet the requirements of long-duration and high-accuracy autonomous navigation, the inertial measurement unit (IMU) requires high cost and large volume. Many biological studies have shown that mantis shrimp [4], desert ants [5], and many other creatures can use the unique visual structure to sense the polarization of skylight and use the polarization information for navigation, foraging, and migration.

Therefore, scholars have been inspired to do lots of research on absolute heading measurement with polarization sensors, which are mainly classified into the point-source type

and image-based type. Although the point-source polarization sensor [6], [7] has achieved high-accuracy navigation performance, it can only obtain a polarization vector of one direction at one time, which could be disturbed easily and has poor robustness. Therefore, image-based polarization sensors have received more and more attention. How to use skylight polarization images to obtain more robust and more accurate navigation information has gradually become a current research hotspot.

A. Heading Measurement With Polarization Sensor

According to the Rayleigh scattering theory [8], the maximum polarization direction of polarized light is always perpendicular to the plane composed of the sun vector and the observation vector. So, the heading can be solved by the difference of the solar azimuth in different coordinate system [9]. Sturzl and Carey [10] and Sturzl [11] used the orthogonality between the polarization vector and the sun vector to solve the solar azimuth by minimizing the vector cross-multiplication results. They further used the polarization vector covariance to improve the accuracy of solar azimuth at a small field of view (FOV). Tang et al. [12] constructed the overdetermined equation about the sun azimuth and altitude, and Jin et al. [9] established the linear analytical model to improve real-time performance. On the other hand, the projection of the solar Meridian on the sensor plane can be directly extracted by using the linear features [13], [14], symmetry [15], or the other image characteristics [1], [16], [17].

Nevertheless, the skylight polarization models of the above heading measurement methods are all Rayleigh models. When the atmospheric turbidity is high and the solar altitude angle changes, the existence of neutral points will significantly affect the robustness of heading measurement. Some studies [18], [19], [20] use the Monte Carlo algorithm to simulate the vector radiation transmission process of sunlight, which improves the characterization performance of the skylight polarization model. But the calculation process is complex and difficult to be applied to the navigation in real time [21]. Berry et al. [22] proposed an analytical model of singular points in the polarization field, which takes into account the neutral points caused by depolarization and reduces the computational complexity. However, there is a certain deviation for the ∞ features of the angle of polarization (AOP) image. Yang et al. [23] improved the representation ability of the Berry model for the degree of polarization (DOP) image by modeling the incident light

intensity under the complex sky, but still did not consider the AOP.

B. Calibration Methods of Polarization Sensor

Except for the changing weather, limited by the manufacturing process, sensor error will also have a great impact on polarization heading measurement, so it is necessary to calibrate the polarization sensor. Han et al. [24] established the error model for CMOS light intensity response error and polarizer installation angle error and used the least-square method to iteratively solve the error parameters. Yang et al. [25] and Liu et al. [26] introduced the coupling coefficient into the error model of the point-source polarization sensor to solve the problem of optical path coupling. Ren et al. [27] introduced the extinction ratio coefficient into the image-based polarization sensor model to unify the incident light intensity of two orthogonal channels, which improved the accuracy of the error parameters. Wan et al. [28] further considered the influence of the main point error of the polarization camera and established the error model based on the Stokes vector. However, the existing calibration methods must be carried out indoors, and expensive instruments such as integrating sphere light sources and cumbersome calibration processes are required.

C. Technical Features

The existing heading measurement methods are all modeled by the single Rayleigh scattering, which cannot adapt to weather conditions with thick aerosols and changing solar altitudes. Moreover, due to the limitation of the manufacturing process, the polarization sensor has problems such as inconsistent light intensity response, installation deviation, and inconsistent extinction ratio of polarizers. These sensor errors will greatly affect the AOP measurement value. Through the calibration of sensor error parameters, AOP measurement values can be corrected, thus improving the accuracy of heading measurement. However, the difficulty of field calibration outdoors lies in that the polarization image cannot separate the error of the sensor from that caused by the complex weather. If directly using the traditional Rayleigh model, the atmospheric environment error and sensor error will be seriously coupled. Therefore, this article proposes a method of heading measurement and field calibration based on the improved Berry model. First, introduce the correction coefficients to the singularity model of the polarization pattern to improve the characterization performance, construct the minimization objective function about the AOP, and use the least-square method to solve the heading robustly. On this basis, the error model of the polarization sensor is established, and the theoretical AOP is calculated by the proposed model and the attitude output from the inertial navigation system (INS). And then estimate the error parameters based on the difference between the measured AOP and the theoretical AOP, to realize the field calibration and improve the heading measurement accuracy. The flowchart of heading measurement and field calibration is shown in Fig. 1. The main features of our method are as follows.
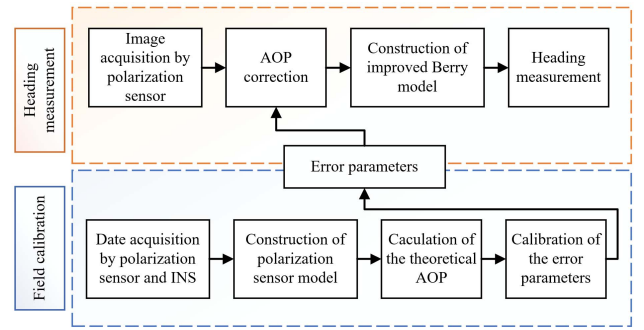

Fig. 1.   Flowchart of heading measurement and field calibration.

1) Using the Berry model that considers the influence of neutral points innovatively to obtain robust heading information.
2) Introduce the correction coefficients to the Berry model to improve the characterization performance of skylight polarization patterns.
3) Propose the field calibration method based on the improved Berry model to separate the sensor error from the polarization model error and improve the heading accuracy.
4) Construct the polarization heading measurement and field calibration system. The attitude output from the INS is used as the prior information of the theoretical AOP, and the advancement is verified in outdoor experiments.

The structure of this article is as follows. Section II introduces the heading measurement method based on the improved Berry model. Section III utilizes the improved Berry model for field calibration. Section IV builds the system of heading measurement and field calibration and carries out simulation and outdoor experiments. Section V summarizes the research work.

II. HEADING MEASUREMENT

A. Skylight Polarization Model

First, we define the coordinate system used in this article.

The navigation coordinate system is the geographic coordinate system. The x-, y-, and z-axes are aligned with the geographic east, north, and zenith directions.

The sensor coordinate system has its origin at the center of the polarization camera's image plane with the z-axis permanent to the image plane and coincides with the sky direction of the navigation coordinate system. The x-axis and y-axis satisfy the right-hand rule.

The observation meridian coordinate system has its origin at the intersection of the observation vector and the celestial sphere. The z_l-axis coincides with the observation vector, and the y_l axis is tangent to the observation meridian plane. The x_l-axis and y_l-axis satisfy the right-hand rule, as shown in Fig. 2(a).

1) Rayleigh Model: Skylight polarization pattern is a special and regular distribution of polarized light generated by the particles scattering of the skylight. In sunny weather, the
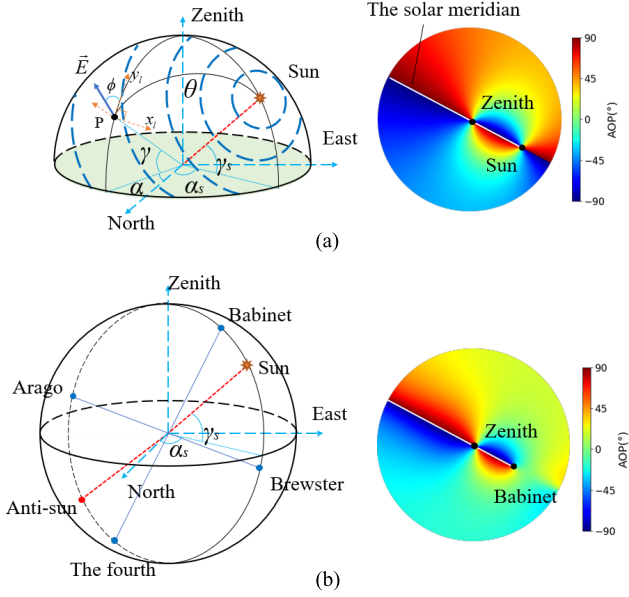
Fig. 2. Schematic of different sky polarization modes. (a) Rayleigh model. (b) Berry model.

scattered particles are mainly composed of atmospheric molecules, the size of which is much smaller than the wavelength of the skylight. Therefore, the single Rayleigh scattering model can be used to describe the atmospheric scattering process: The E vector (the electric vibration vector in the light wave) of the scattered light is perpendicular to the scattering surface. As shown in Fig. 2(a), O represents the position of the observer, S represents the position of the sun on the celestial sphere, and the zenith angle and azimuth angle are γ_s and α_s, respectively. P represents the observation position, and the zenith angle and azimuth angle are γ and α, respectively. ϕ is the polarization angle of incident light and θ is the scattering angle. Thus, the skylight polarization information based on the Rayleigh scattering model can be obtained as

$$d = \frac{\sin^2\theta}{1 + \cos^2\theta} \tag{1}$$

$$\tan\phi = \frac{\cos\gamma_s \sin\gamma - \sin\gamma_s \cos\gamma \cos(\alpha - \alpha_s)}{-\sin(\alpha - \alpha_s)\sin\gamma_s} \tag{2}$$

where d represents the DOP and ϕ represents the AOP.

2) Berry Model: However, the actual atmospheric polarization mode does not strictly meet the single Rayleigh scattering model, and there will be obvious "neutral points" in the polarization distribution diagram, which will seriously affect the robustness of the heading measurement. This depolarization effect is caused by multiorder scattering, anisotropic scattering, and ground reflection of aerosol particles. The four neutral points are located on the main plane that is perpendicular to the sun and the zenith [29], and their distribution is shown in Fig. 2(b). The Babinet and Brewster are located on both sides of the Sun, while Arago and the Fourth are located on both sides of the anti-Sun.

Berry et al. [22] proposed the singularity theory of polarization field to model the neutral points. To quantitatively describe the sky polarization information, use the Cartesian coordinate

system to represent the projection of an observation vector $OP(x, y, z)$ on the celestial sphere, and its altitude angle is β. The complex form on the ground plane is $\zeta = x + iy$ and that in the polar coordinate system is $\zeta = r \exp(i\delta)$. And set the antisymmetric point of ζ as $-1/\zeta^*$. The polarization information can be expressed in the complex form of nonnormalized Stokes parameters E_x and E_y as

$$w(\zeta) = \left\langle \left(E_x + iE_y\right)^2 \right\rangle = |w(\zeta)| \exp(2i\phi(\zeta)) \tag{3}$$

where $|w(\zeta)|$ represents the DOP, and $\phi(\zeta)$ contains the polarization angle information relative to the x-axis direction. $w(\zeta)$ is the function related to the observation vector, and the zero points of the function can be expressed as the neutral points of the skylight polarization pattern. To account for the effects of atmospheric multiple scattering, the coefficient of atmospheric turbidity is set as A. If the projection line of the solar meridian always coincides with the y-axis and the Sun altitude is β_s, the projection point of the sun on the ground plane is $\zeta_s = iy_s = i(1 - \tan(\beta_s/2))/(1 + \tan(\beta_s/2))$. Then, the four neutral points are

$$\zeta_+ = i\frac{(y_s + A)}{(1 - Ay_s)}, \quad \zeta_- = i\frac{(y_s - A)}{(1 + Ay_s)}, \quad -1/\zeta_+^*, \quad -1/\zeta_-^* \tag{4}$$

where $y_s = (1 - \tan(\beta_s/2))/(1 + \tan(\beta_s/2))$ represents the distance between the Sun projection point and the origin, ζ_+ and ζ_- are on both sides of the Sun vector, while $-1/\zeta_+^*$ and $-1/\zeta_-^*$ are on both sides of the anti-Sun vector. The angular distance between two adjacent neutral points is $\varepsilon = \arctan A$. And set the projection length of the observing vector OP is $r = (1 - \tan(\beta/2))/(1 + \tan(\beta/2))$. To make the DOP also meet $|w(\zeta)| = |w(1/\zeta^*)|$, the above formula is further modified as

$$w(\zeta) = -\frac{4(\zeta - \zeta_+)(\zeta - \zeta_-)(\zeta + 1/\zeta_+^*)(\zeta + 1/\zeta_-^*)}{(1 + r^2)^2 |\zeta_+ + 1/\zeta_+^*||\zeta_- + 1/\zeta_-^*|}. \tag{5}$$

B. Improved Berry Model

The Berry model considers the influence of a turbid atmosphere. However, it is established under the condition that the solar meridian coincides with the yoz-plane, which is difficult to be applied to navigation. In addition, Fig. 2(b) shows that the shape saturation of the Berry model is still different from Rayleigh, which will have a certain impact on the heading measurement. Therefore, the improved Berry model is proposed to characterize the skylight polarization.

Set the atmospheric turbidity constant as A and the solar altitude angle in the polarization sensor coordinate system as β, then the projection point of the solar vector is $y_m = (1 - \tan(\beta/2))/(1 + \tan(\beta/2))$, and the coordinates of the neutral points in (4) are expressed in matrix form

$$\zeta^T = \begin{bmatrix} 0 & 0 & 0 & 0 \\ i\frac{(y_m + A)}{(1 - Ay_m)} & i\frac{(y_m - A)}{(1 + Ay_m)} & i - \frac{(1 - Ay_m)}{(y_m + A)} & i - \frac{(1 + Ay_m)}{(y_m - A)} \end{bmatrix}. \tag{6}$$

The solar azimuth in the sensor coordinate system at the current time is set as α, so the 2-D rotation matrix on the ground plane is defined as

$$R_{\text{Berry}} = \begin{bmatrix} \cos(\alpha/2) & -\sin(\alpha/2) \\ \sin(\alpha/2) & \cos(\alpha/2) \end{bmatrix}. \tag{7}$$

Then rotate the neutral point vector in the ground plane to obtain the neutral point coordinate at the current time as

$$\begin{bmatrix} \zeta_1 & \zeta_2 & \zeta_3 & \zeta_4 \end{bmatrix} = R_{\text{Berry}} \boldsymbol{\zeta}^T. \tag{8}$$

In addition, the projection points $\zeta = x + iy$ of the observation vector $OP(x, y, z)$ in the initial state are also rotated to obtain the coordinates of the projection points ζ under the sensor coordinate system

$$\boldsymbol{\zeta}_{\text{Berry}} = \begin{bmatrix} x_{\text{Berry}} & i y_{\text{Berry}} \end{bmatrix}^T = R_{\text{Berry}} \begin{bmatrix} x & iy \end{bmatrix}^T. \tag{9}$$

If the initial observation projection point ζ is known, (9) can be brought into formula (5) to obtain the sky polarization mode constraints based on the Berry model for solar azimuth α, altitude β, and atmospheric turbidity parameters A as follows:

$$w(\boldsymbol{\zeta}_{\text{Berry}}) = w(\alpha, \beta, A) \propto (\zeta - \zeta_1)(\zeta - \zeta_2)(\zeta - \zeta_3)(\zeta - \zeta_4). \tag{10}$$

In order to make the shape saturation closer to the measured value, this article introduces the correction coefficient k_1 and k_2 to correct the positions of neutral points on both sides of the anti-Sun. Then the corrected neutral point coordinates can be expressed as

$$\begin{bmatrix} \zeta_1 & \zeta_2 & \zeta_3{}' & \zeta_4{}' \end{bmatrix} = \begin{bmatrix} 0 & 0 & 0 & 0 \\ \zeta_+ & \zeta_- & -k_1/\zeta_+{}^* & -k_2/\zeta_-{}^* \end{bmatrix}. \tag{11}$$

Substitute (11) into formula (5) to obtain the real-time characterization function of sky polarization based on the improved Berry model

$$w(\alpha, \beta, A, k_1, k_2) = -\frac{4(\zeta - \zeta_1)(\zeta - \zeta_2)(\zeta - \zeta_3{}')(\zeta - \zeta_4{}')}{(1 + r^2)^2 |\zeta_1 - \zeta_3{}'||\zeta_2 - \zeta_4{}'|}. \tag{12}$$

C. Heading Measurement Based on the Improved Berry Model

After the skylight polarization model is established, heading solving is the most important part. The imaging process of the skylight polarization pattern by the polarization sensor is shown in Fig. 3, and the internal parameters and distortion of the fisheye camera are calibrated by [30]. Each pixel (u, v) of the polarization sensor corresponds to an observation vector $OP_i(x, y, z)$ and a polarization vector $\vec{E}_i$, as shown in Fig. 3(a). Then the polarization angle ψ_i and degree d_i under the senor coordinate system are

$$\psi_i(\mathbf{x}) = \frac{1}{2}\arctan(\text{imag}(w_i(\mathbf{x})), \text{real}(w_i(\mathbf{x}))), d_i = |w_i(\mathbf{x})| \tag{13}$$

where $\mathbf{x} = [\alpha, \beta, A, k_1, k_2]^T$ represents parameters of the sun position and the atmospheric turbidity. $\text{imag}(\cdot)$ and $\text{real}(\cdot)$
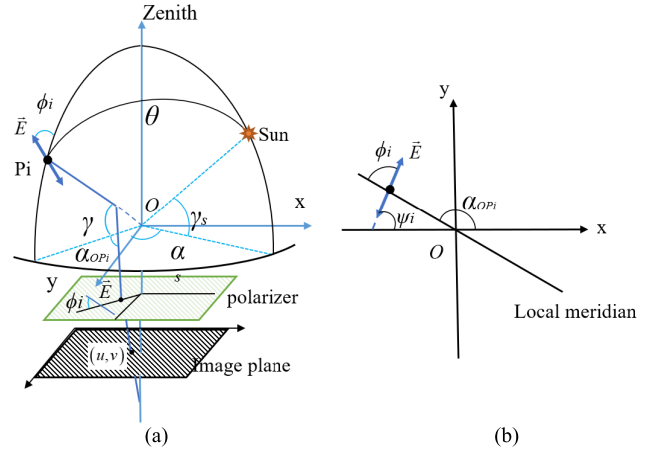

Fig. 3. Schematic of the imaging process of the image-based polarization sensor. (a) E vector in the observation meridian coordinate system. (b) E vector in the sensor coordinate system.

denote the imaginary and real parts of the complex number, respectively. To obtain the AOP information under the observation meridian coordinate system, the conversion is required [31]

$$\phi_i(\mathbf{x}) = \psi_i(\mathbf{x}) - \alpha_{OPi}. \tag{14}$$

As shown in Fig. 3(b), ψ_i represents the AOP under the sensor coordinate system and α_{OPi} represents the azimuth of the current observation vector. The measured value of AOP also needs to be processed $\phi_{mi} = \psi_{mi} - \alpha_{OPi}$. ψ_{mi} is the measured value under the sensor system and ϕ_{mi} is that under the observation meridian coordinate system. If the number of pixels is N, the minimization objective function can be constructed

$$\mathbf{x} = \arg\min_{\mathbf{x}} \left(\sum_{i=1}^{N} \|\phi_i(\mathbf{x}) - \phi_{mi}\| \right). \tag{15}$$

The objective function is solved by Powell [32] algorithm to obtain the estimated solar azimuth α in the sensor coordinate system. According to the local geographical location and time, the solar azimuth α_s in the navigation coordinate system can be obtained. Then the heading can be calculated by the difference between α and α_s as

$$\begin{cases} \text{head}_1 = \alpha - \alpha_s \\ \text{head}_2 = \alpha - \alpha_s + \pi \end{cases} \tag{16}$$

where head_1 and head_2 are the final calculated heading values. There is 180° ambiguity in the heading solution, which can be determined in combination with other navigation systems.

III. FIELD CALIBRATION

Limited by the manufacturing process, the performance of the image-based polarization sensor is largely restricted by the error calibration parameters. Nevertheless, the traditional indoor calibration method needs expensive instruments and a complex calibration process, and the characterization performance of the skylight polarization model is very important to
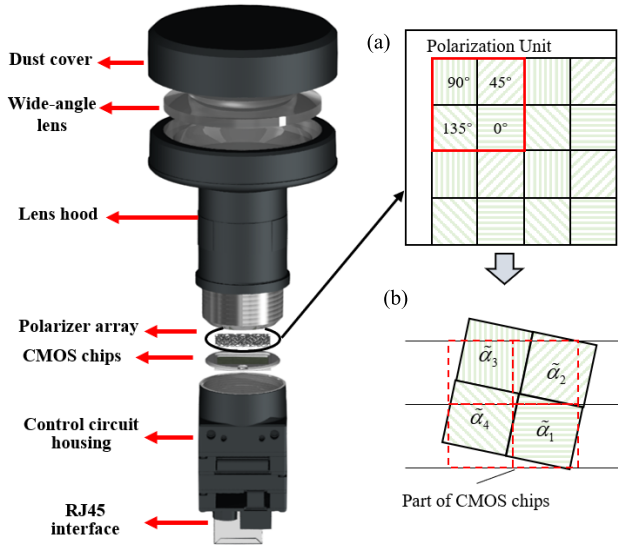
Fig. 4. Schematic of the structure of the image-based polarization sensor. (a) Single polarization unit. (b) Installation error between the polarizer and the CMOS chip.

the effect of field calibration. Therefore, this article proposes a field calibration method based on the improved Berry model. First, the error model of the image-based polarization sensor is constructed, and then the AOP theoretical values of the improved Berry model are calculated with the attitude information output from the INS, and finally, the error parameters can be estimated in combination with the measured AOP images.

A. Image-Based Polarization Sensor Model

The polarization sensor built in this study is mainly composed of Fujinon FE185C057HA-1 fisheye lens and LUCID PHXET050S-P polarization camera, as shown in Fig. 4. The scattered light in the atmosphere is incident on the array polarizing unit after passing through the wide-angle lens and the lens hood. Each polarization unit consists of four adjacent pixel channels, and the polarizer installation directions of the corresponding channels are 0°, 45°, 90°, and 135°, respectively. The scattered light will be imaged on the CMOS chip after passing through the polarization units. Each polarization sensor contains 2048 × 2448 channels, and the size of each pixel channel is 3.45 × 3.45 μm. The main sources of polarization sensor error are the inconsistency error of light intensity response, the installation error of the polarizer and the inconsistency error of extinction ratio coefficient.

According to Marius law [33], the light intensity response value of the pixel channel in the ith polarization unit can be expressed as

$$Ip_k = 0.5I[1 + d\cos(2\psi - 2\alpha_k)], \quad k = 1, \ldots, 4 \quad (17)$$

where d represents the DOP, Ip_k represents the light intensity value of the pixel channel with polarizer installation angles of 0°, 45°, 90°, and 135°, respectively; I represents the light intensity of the incident light; d represents the DOP of the incident light; ψ represents the AOP under the polarization sensor system; α_k is the polarizer mounting angle of the pixel

channel. Therefore, the polarization state can be described by the Stokes vector as $\tilde{s} = [s_0 \ s_1 \ s_2]^T$. So, the measured polarization angle and polarization degree of the polarization unit are $\psi_i = 0.5\arctan(s_2, s_1)$ and $d_i = (s_1^2 + s_2^2)^{1/2}/s_0$. The accuracy of DOP is largely affected by the extinction ratio coefficient of the polarizer [32]. However, the extinction ratio coefficients of different polarizers cannot be completely consistent, resulting in a certain deviation of DOP. In addition, the misalignment of the installation between the array polarizer and the CMOS chip will also lead to the coupling of the optical path, which affects the measurement accuracy of the polarization information, as shown in Fig. 4(b). Moreover, different polarization channels of the array polarization units will also produce different degrees of attenuation to the incident light. Therefore, the error propagation model is established as

$$Ip_k = \beta_k I[1 + \eta_k d\cos(2\psi - 2\tilde{\alpha}_k)] \quad (18)$$

where β_k is the attenuation parameter of the incident light intensity of the kth pixel channel, $\tilde{\alpha}_k$ is the installation angle of the polarizer with error, and η_k is the parameter of the inconsistency error of the extinction ratio coefficient.

Due to the difference between photodiodes and the thermal effect of circuits, the photosensitive response intensity of each pixel channel on the CMOS chip is inconsistent. Therefore, further considering the photosensitivity consistency error, the relationship between the incident light intensity and the CMOS response light intensity is modeled as

$$Icmos_k = \lambda_k Ip_k + \delta_k \quad (19)$$

where λ_k is the light intensity response proportional coefficient of the kth pixel channel of the CMOS chip, δ_k is the bias coefficient, $Icmos_k$ is the light intensity response value of the pixel channel, and Ip_k is the output light intensity passing through the polarizers. Therefore, (18) and (19) are the error model of the polarization sensor in this study.

B. Objective Function

After establishing the error model of the bionic polarization sensor, the parameters to be calibrated mainly include the CMOS photosensitive consistency error parameters λ_k and δ_k, and the array polarizer error parameters β_k, η_k, and $\tilde{\alpha}_k$. Set the CMOS response vector of the polarization unit to be $[Icmos_1, Icmos_2, Icmos_3, Icmos_4]^T$, then according to (19), the polarization response vector can be expressed as

$$\tilde{\mathbf{I}} = \begin{bmatrix} Ip_1 \\ Ip_2 \\ Ip_3 \\ Ip_4 \end{bmatrix} = \begin{bmatrix} 1/\lambda_1 \\ 1/\lambda_2 \\ 1/\lambda_3 \\ 1/\lambda_4 \end{bmatrix} \left(\begin{bmatrix} Icmos_1 \\ Icmos_2 \\ Icmos_3 \\ Icmos_4 \end{bmatrix} - \begin{bmatrix} \delta_1 \\ \delta_2 \\ \delta_3 \\ \delta_4 \end{bmatrix} \right). \quad (20)$$

According to the array polarizer error model (18), the relationship between the corrected Stokes vector $\tilde{s}$ and the polarization response $\tilde{\mathbf{I}}$ can be expressed as the form of a matrix as

$$\tilde{\mathbf{I}} = \begin{bmatrix} Ip_1 \\ Ip_2 \\ Ip_3 \\ Ip_4 \end{bmatrix} = \mathbf{H}\tilde{s} = \begin{bmatrix} \beta_1 & \eta_1\beta_1\cos 2\tilde{\alpha}_1 & \eta_1\beta_1\sin 2\tilde{\alpha}_1 \\ \beta_2 & \eta_2\beta_2\cos 2\tilde{\alpha}_2 & \eta_2\beta_2\sin 2\tilde{\alpha}_2 \\ \beta_3 & \eta_3\beta_3\cos 2\tilde{\alpha}_3 & \eta_3\beta_3\sin 2\tilde{\alpha}_3 \\ \beta_4 & \eta_4\beta_4\cos 2\tilde{\alpha}_4 & \eta_4\beta_4\sin 2\tilde{\alpha}_4 \end{bmatrix} \tilde{s}. \quad (21)$$

$\tilde{\mathbf{s}} = [s_0 \ s_1 \ s_2]^T = [I \ Id^c \cos 2\psi^c \ Id^c \sin 2\psi^c]^T$ represents the polarized Stokes vector after correction, ψ^c and d^c represents the corrected AOP and DOP, respectively; and $\mathbf{H}$ represents the calibration coefficient matrix of the array polarizer error model. Since the coefficient matrix cannot be inverted, use the least-squares method to solve $\tilde{\mathbf{s}} = (\mathbf{H}^T \mathbf{H})^{-1} \mathbf{H}^T \tilde{\mathbf{I}}$.

Therefore, obtaining the calibrated polarization angle and polarization degree

$$\psi^c = 0.5 \arctan(s_2/s_1), \quad d^c = \sqrt{s_1^2 + s_2^2}/s_0. \quad (22)$$

Then according to formula (14), the AOP is converted into the coordinate system of the observation meridian plane as ϕ^c. If M polarized images are obtained, each image has N polarized units, and the ith polarized unit of each image is used as the calibration vector, to obtain the CMOS response vector group $\mathbf{Q}$ and the theoretical AOP vector $\mathbf{\Phi}^{\text{sim}}$ of the ith polarized unit

$$\mathbf{Q} = [\tilde{\mathbf{I}}_1, \ldots, \tilde{\mathbf{I}}_M]_{4 \times M}, \quad \mathbf{\Phi}^{\text{sim}} = [\phi_1^{\text{sim}}, \ldots, \phi_M^{\text{sim}}]_{1 \times M}. \quad (23)$$

The parameters to be calibrated are

$$\mathbf{y} = \{\lambda_k, \delta_k, \beta_k, \eta_k, \tilde{\alpha}_k | k = 1, 2, 3, 4\}. \quad (24)$$

If more than 20 AOP images and simulation values of typical positions are obtained, 20 calibration parameters can be solved. Q provides a group of AOP corrections $\Phi^c = [\phi_1^c, \ldots, \phi_M^c]_{1 \times M}$. Expressing the corrected AOP $\phi_m^c(\mathbf{y})$ as a function about the calibration parameters $\mathbf{y}$, then the error parameters can be solved by the minimum objective function (25) between the AOP correction value and the theoretical value, which is also solved by Powell [32] algorithm

$$\mathbf{y} = \arg\min_{\mathbf{y}} \left(\sum_{m=1}^{M} \|\phi_m^{\text{sim}} - \phi_m^c(\mathbf{y})\| \right). \quad (25)$$

If more than 20 AOP images and simulation values of typical positions are obtained, 20 calibration parameters can be solved.

C. Field Calibration Based on Improved Berry Model

Although the objective function to minimize the difference between the measured AOP and the theoretical AOP is proposed above, if the Rayleigh model is directly used, it will cause serious coupling between the sky polarization model error and the sensor error. Therefore, the field calibration method based on the improved Berry model is proposed. The specific steps are as follows.

Step 1: First, the polarization sensor and INS are fixed on the aluminum alloy bracket, and after leveling, the calibration device is rotated every $\Delta°$ to obtain M groups of AOP images in different heading states. And each image corresponds to an attitude value $[\text{pitch}_m, \text{roll}_m, \text{head}_m]^T$ of the INS, representing the pitch, roll and heading values of the mth heading state of INS. If each image has N pixels involved in the calculation, the group of CMOS response vector $\{\tilde{\mathbf{I}}_{mi}\}_{m,i=1}^{M,N}$ set can be obtained.

Step 2: Then construct the theoretical AOP image in M states. Combined with the local geographic location and time, the solar altitude β_m^s and azimuth α_m^s in the navigation

coordinate system of the mth picture are calculated, and then according to (26), the theoretical values of the solar elevation β_m^{sim} angle and azimuth α_m^{sim} angle under the sensor coordinate system can be obtained as

$$\begin{cases} \alpha_m^{\text{sim}} = \alpha_m^s - \text{head}_m \\ \beta_m^{\text{sim}} = \beta_m^s. \end{cases} \quad (26)$$

Substitute the measured AOP group $\{\phi_{mi}\}_{m=1}^M$ of the mth image into the improved Berry model (15), in which the fit atmospheric turbidity parameter is $[A_m, k_{1m}, k_{2m}]$, then the complex representation of the polarization information of the current heading state is $\{w_{mi}(\alpha_m^{\text{sim}}, \beta_m^{\text{sim}}, A_m, k_{1m}, k_{2m})\}_{i=1}^N$, so the theoretical AOP value is $\{\phi_{mi}^{\text{sim}}\}_{m,i=1}^{M,N}$.

Step 3: Finally, carry out the calibration of the polarization sensor. Substituting the CMOS response vector $\{\tilde{\mathbf{I}}_{mi}\}_{m=1}^M$ of the polarization unit with the same index of each picture and the theoretical AOP $\{\phi_{mi}^{\text{sim}}\}_{m=1}^M$ into the formula (25), the error parameters of the ith polarization unit can be solved by minimizing the objective function. The loop iterates until all the polarization units in the target area complete the calibration and obtain a set of sensor error parameters $\{\mathbf{y}_i\}_{i=1}^N$.

IV. EXPERIMENTS

To verify the effectiveness of the improved Berry model in heading measurement and field calibration, the outdoor experiment was carried out on March 9, 2022, and August 17, 2022, on the rooftop of the Technology Innovation Building of Harbin Institute of Technology (longitude 126.6236°, latitude 45.7261°, altitude 148.74 m). The first group of data was collected from 15:30 to 15:40 on March 9. On August 17, we collected another six groups. The single experiment time is also less than 10 min. The solar altitude angle of the data at 9:00 and 10:00 is 40°–50° and that of the data at 14:30, 15:30, 16:30, and 17:00 is 20°–30°. The experimental system is shown in Fig. 5. The polarization sensor and the fiber INS (FINS) are fixed on the alloy bracket, and the damping tripod is used as the support to adjust the attitude of the polarization sensor during the data acquisition process. The instrument specifications are shown in Table I. The gyro bias stability of FINS is 0.02°/h, and the attitude accuracy can be within 0.1° combined with GPS. In this experiment, we input the location information directly to FINS instead of the GPS antennas. After the system was powered on, the initial alignment of FINS was performed first, and then the leveling is performed according to the attitudes output from the FINS, and the pitch and roll misalignment are controlled within 1°. The polarization sensor is then manually rotated every 10° and ten images are acquired each time. Thereby, 360 skylight polarization images are obtained for each experiment. Using the collected AOP images, the heading measurement and the field calibration are carried out.

We evaluate the field calibration and heading measurement performance of different models by the STD of the error between the heading measurement value and the FINS output value. However, due to the existence of FINS initial alignment and installation errors, the error of heading measurement is not unbiased, and the mean error $\bar{E}$ is not zero. Therefore,
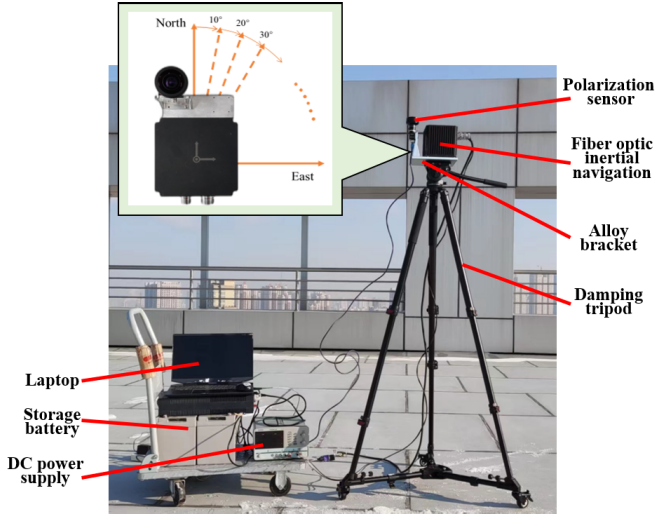
Fig. 5. Schematic of the experimental system and process flow.

Fig. 6. Simulation and measurement results of skylight polarization pattern.

TABLE I

INSTRUMENT SPECIFICATIONS

Device name	Device model	Parameters	
Lucid polarization camera	PHXET050S-P	Resolution: 2048 x2448, Frame rate: 22FPS	
Fujinon fish eye Lens	FE185C057HA	Focal length: 1.8mm, view: 185.0° x 185.0°	
FINS	FINS150	Accelerometer	Bias: 0.05 mg,
		Gyro	Bias: 0.02°/h, Random walk: $0.002°/\sqrt{h}$
		Heading	0.1°(GPS)

TABLE II

COMPARISON OF SIMILARITY COEFFICIENTS OF DIFFERENT MODELS

Heading	Rayleigh	Berry	Proposed
0°	68.28%	38.50%	**83.33%**
90°	81.55%	44.05%	**87.71%**
180°	64.78%	31.84%	**80.56%**
270°	82.77%	50.02%	**87.64%**
Average	74.34%	41.10%	**84.81%**

to eliminate the influence of constant deviation, we use the relative change of heading to evaluate the model performance and subtract this mean value

$$\text{STD} = \sqrt{\frac{\sum_{m=1}^{M} \left(\text{head}_m - \text{head}_m^{\text{FINS}} - \bar{E}\right)^2}{M}}. \quad (27)$$

where $\bar{E} = (\bar{E}_{\text{Berry}} + \bar{E}_{\text{proposed}})/2$, and $\bar{E}_{\text{Berry}}$ and $\bar{E}_{\text{proposed}}$ are the mean of error of Berry model and improved Berry model, respectively. head_m and $\text{head}_m^{\text{FINS}}$ are heading measurement value and FINS output value, respectively. M represents the number of pictures collected.

A. Characterization Performance

To verify the characterization performance of the improved Berry model compared with the traditional skylight polarization model, four groups of AOP images at 15:30 on March 9 with different heading values are used to carry out the characterization performance experiment. Represented by the heading of 0°, 90°, 180°, and 270°, the actual AOP images detected by the polarization sensor, as well as the theoretical AOP images simulated by Rayleigh model, Berry model, and proposed model are shown in Fig. 6. The atmospheric turbidity parameter A is set to 25°, the correction coefficients k_1 and k_2 are set to 1.5 experientially. It shows that the ∞ shape
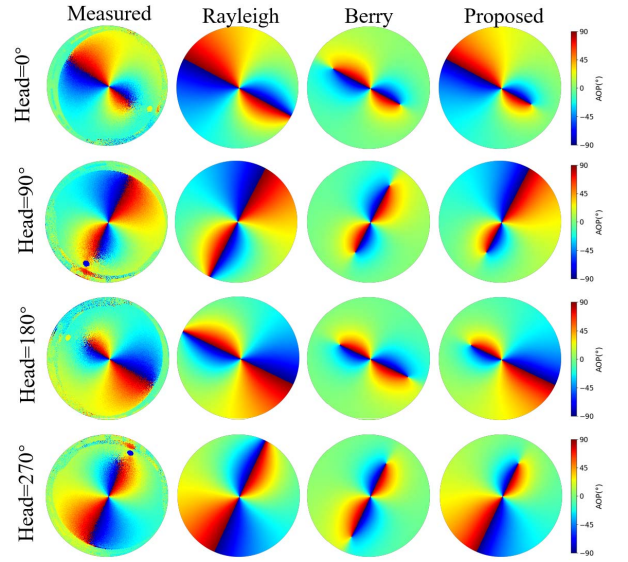
of the Rayleigh model in the central area is similar to the measured value, but since the polarization neutral points are not considered, the AOP value near the sun position is quite different from the measured value. As for the Berry model, the AOP zero-point position represents the neutral point position, and this is more consistent with the measured value, but the saturation of the ∞ shape is still quite different. However, the proposed model not only includes the position information of the neutral points, but also controls their position through the polarization correction coefficient, which has a high consistency with the measured AOP image.

To further quantitatively evaluate the characterization performance of the polarization model, refer to RN6, calculate the difference ($|\text{AOP}_1 - \text{AOP}_2| = \nabla\text{AOP}$) between the simulated AOP and the measured AOP of each polarization unit. When ∇AOP is less than 10°, this polarization unit is considered to be the approximate one. Use N_{similar} and N_{total} to denote the approximate number and the total number of polarization units, respectively. Definition ε as the similarity coefficient

$$\varepsilon = N_{\text{similar}}/N_{\text{total}}. \quad (28)$$

The statistical results of the similarity coefficient of different models in different heading states are shown in Table II. The similarity coefficient of the improved Berry model proposed in this article is better than both the Rayleigh model and Berry model in different heading states. The average of AOP image similarity coefficient is 106.35% higher than the Berry model
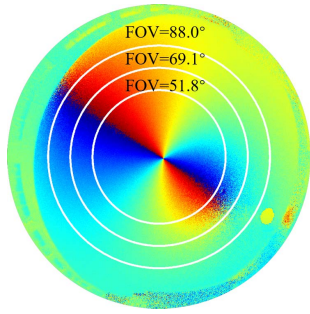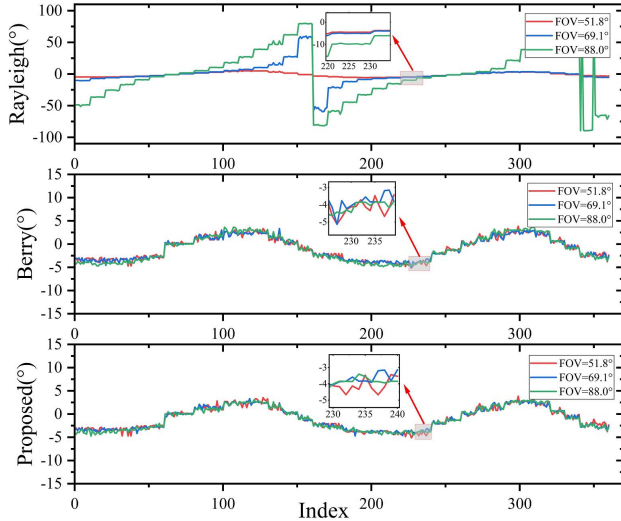
Fig. 7.   Schematic of different FOV.

Fig. 9.   Error comparison of heading measurement of different models at 10:00 on August 17, 2022.

Fig. 8.   Error comparison of heading measurement of different models at 15:30 on March 9, 2022.

TABLE III
COMPARISON OF HEADING ERRORS STD (°) FOR DIFFERENT FOV

Time	Model	FOV=51.8°	FOV=69.1°	FOV=88.0°
15:30 on March 9	Rayleigh	3.2823	15.5903	40.8613
	Berry	2.3982	2.3688	2.7101
	Proposed	**2.3780**	**2.3500**	**2.4386**
10:00 on August 17	Rayleigh	38.1966	30.6915	28.8438
	Berry	4.1803	3.4828	3.2099
	Proposed	**4.1673**	**3.1927**	**2.5925**

and 14.08% higher than the Rayleigh model, which verifies the superiority of the proposed model.

B. Heading Measurement With Different FOV

Heading measurement is further performed on two sets of images collected at 15:30 on March 9 and 10:00 on August 17, respectively. As shown in Fig. 7, three areas with FOV sizes of 51.8°, 69.1°, and 88.0° are selected randomly, and the heading of each image is calculated by different skylight polarization models. The heading calculation method based on the Rayleigh model refers to the least-square method proposed in [10]. The heading errors are shown in Figs. 8 and 9. The comparison of heading errors STD (°) calculated for different FOV is shown in Table III.

As for the Rayleigh model, as the size of FOV increases, the solution results are unstable and even incorrect. However, the Berry model and the proposed model is more robust with different size of FOV. This is because, with the increase of the FOV, the area affected by the depolarization effect gradually becomes larger, which destroys the characteristics of the Rayleigh model and leads to erroneous solutions. However, the Berry model considers neutral points generated by multiple scattering of atmospheric aerosol particles and
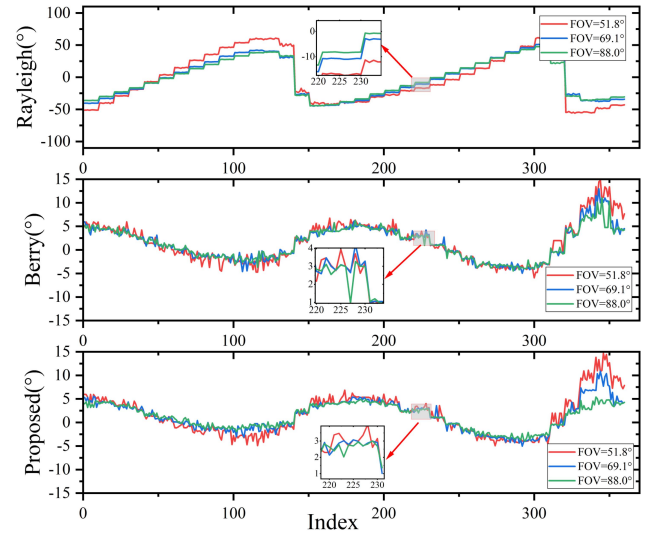
can still calculate correct navigation information even if the atmosphere is turbid.

Table III shows that even under the same FOV, the STD of the heading error of the improved Berry model relative to FINS is still smaller compared with the Berry model. The improvement is particularly noticeable when the Sun is high (10:00 on August 17, 2022). This is because the depolarization effect becomes more obvious with the increase in solar altitude. And the proposed model can adjust the saturation of the AOP image by controlling the neutral point position of anti-Sun vector through the neutral point correction coefficient, which is closer to the measured AOP and improves the robustness of heading measurement.

C. Field Calibration

In practical applications, due to the limitations of the manufacturing process, the AOP measurement accuracy will be greatly affected by manufacturing errors. To verify the advantages based on the improved Berry model, 360 AOP images collected at 15:30 on March 9 are used for the field calibration experiments. The light intensity response error parameters, polarizer installation error parameters, and extinction ratio error parameters of all pixel channels within the $FOV = 88°$ are calibrated. Refer to the ideal CMOS response formula (17), set the initial value of the parameters
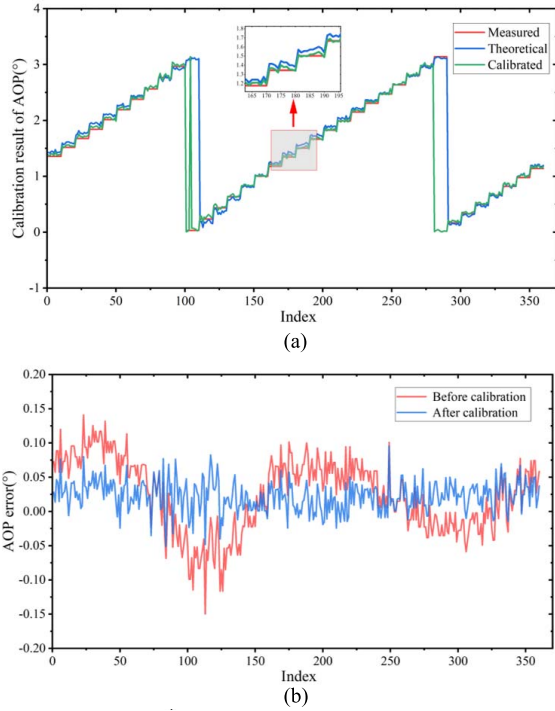
Fig. 10. Error comparison of heading measurement of different models. (a) Calibration results. (b) AOP error after calibration.

Time	Rayleigh(°)	Berry(°)	Proposed(°)
09:00	27.7718	1.4098	**1.0326**
10:00	27.9003	1.9706	**1.2611**
14:30	6.5753	0.7157	**0.7015**
15:30	4.5729	0.8366	**0.7903**
16:30	1.1526	0.8073	**0.7142**
17:00	1.4351	0.5331	**0.4648**
Average	11.5680	1.0455	**0.8274**

$$\mathbf{y} = \{\lambda_k, \delta_k, \beta_k, \eta_k, \tilde{\alpha}_k | k = 1, 2, 3, 4\} \text{ to be calibrated as}$$

$$\mathbf{y}_{\text{init}} = [1, 1, 1, 1, 0, 0, 0, 0, 0.5, 0.5, 0.5, 0.5$$
$$1, 1, 1, 1, 0, \pi/4, \pi/2, 3\pi/4]. \quad (29)$$

Then select the boundaries of the error parameters in the objective function optimization process. Set the variation range of the light intensity response proportional coefficient λ_k, extinction ratio coefficient η_k, and light intensity attenuation coefficient β_k to 90% to 110% of the ideal state, so the selected boundaries are, respectively, [0.9 1.1], [0.9 1.1] and [0.45 0.55]. The response bias coefficient δ_k is ±10% of the maximum normalized light intensity, and the selected boundary is [−0.1 0.1]; the polarizer installation parameter of single channel fluctuates by ±5° around the theoretical value. Finally, the objective function is optimized according to the initial values and boundaries, and the error parameters could be solved. The AOP value and error value of a single polarization unit before and after calibration are shown in Fig. 10. The measured AOP before calibration has a large periodic error relative to the theoretical value. After calibration, the error is significantly reduced, and the periodic error is well suppressed. Therefore, the proposed method can well overcome the influence of the sensor error on AOP measurement and improve the AOP accuracy.

D. Heading Measurement With Changing Weather

Furthermore, verify the heading robustness of the field calibration results based on the improved Berry model with changing solar altitude. We conduct heading measurement experiments on the six groups' images collected on August 17.

The polarization images are corrected using the polarization sensor error parameters calibrated in the last subsection, and the FOV is also set to 88.0°. For the calibration results of the Rayleigh, Berry, and improved Berry models, the headings are solved based on the Rayleigh model, Berry model, and improved Berry model, respectively.

Finally, compared with the heading value output from FINS, the heading error is shown in Fig. 11. The heading measurement accuracy is evaluated by the STD value of heading error, as shown in Table IV.

With the decrease in solar altitude, the heading measurement error of all models decreases gradually. This is because the depolarization effect becomes weaker as the solar altitude angle decreases, so the influence on heading measurement becomes smaller. However, the heading measurement after field calibration based on the Rayleigh model has large fluctuations, while that based on the Berry model or the proposed model are stable with smaller heading errors. When the solar altitude is low and the depolarization effect is weak, such as in the 16:30 and 17:00 data, the Rayleigh model can obtain reliable heading results after field calibration, but it is still not as good as the proposed model. Moreover, due to the reflection of sunlight on the ground and buildings, the distance between the neutral point of the AOP image and the center in a single experiment is uneven. The heading measurement and field calibration based on the Rayleigh model cannot adapt to this change, which leads to some jump points of heading errors, as shown in Fig. 11(c) and (f). However, the Berry model and the improved model can fit the neutral points to avoid this phenomenon. Besides, since the Rayleigh model does not consider the influence of aerosol depolarization, when the solar altitude rises, the position of the neutral points also changes, which destroys the characteristic features of the Rayleigh model, resulting in lower heading accuracy. Berry model and the proposed model both consider the neutral points, which can well adapt to the change in the solar altitude. Moreover, the improved Berry model can well correct the ∞ shape saturation of the AOP image, so higher-accuracy results are obtained. With the decline of the solar altitude, the heading measurement errors of the Berry model and the proposed model are gradually approaching. This is because the influence of atmospheric depolarization effect on AOP measurement value gradually decreases. However, the improvement is especially obvious when the solar altitude is high, such as in the data of 9:00 and 10:00. This is because the adaptability to the depolarization effect of the Berry model
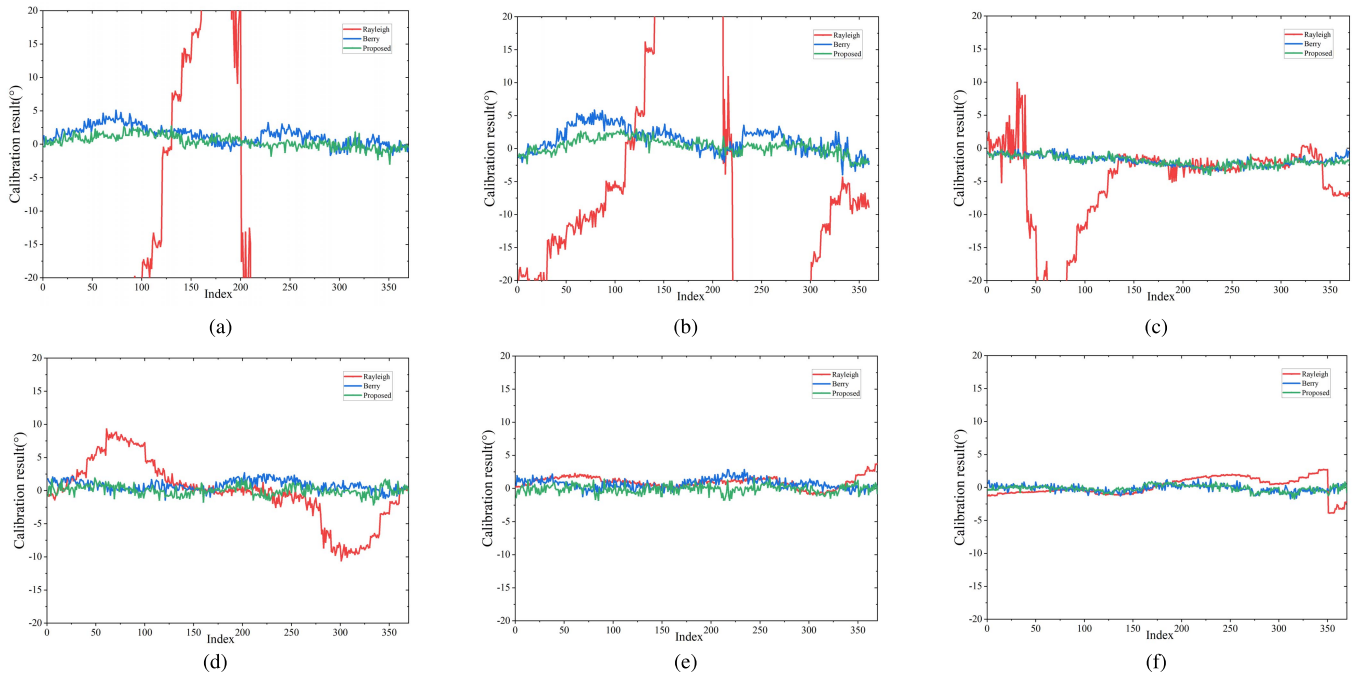
Fig. 11. Heading error after field calibration at different times. (a) 2022-08-17 9:00. (b) 2022-08-17 10:00. (c) 2022-08-17 14:30. (d) 2022-08-17 15:30. (e) 2022-08-17 16:30. (f) 2022-08-17 17:00.

gradually weakens when the solar altitude increases. The proposed model can better improve the robustness of heading measurement and field calibration due to the introduction of correction coefficients. The last row of Table IV shows the average value of heading error STD of six groups of data with different methods. And we use the reduction ratio as the evaluation index $(\overline{STD}_{tra} - \overline{STD}_{pro})/\overline{STD}_{tra} \times 100\%$, $\overline{STD}_{tra}$ is the average STD of the traditional method, and $\overline{STD}_{pro}$ is the average STD of the proposed method. Compared with the traditional Berry model and Rayleigh model, the average STD of the heading error is reduced by 20.86% and 92.85%, respectively, which verifies the advantages and broad application prospects of the proposed method.

V. CONCLUSION

Aiming at the problem of poor robustness of the existing methods for polarization heading measurement due to the insufficient characterization performance of skylight polarization modes, this article proposed a new method of heading measurement based on the Berry model. First, the neutral points generated by the depolarization of the turbid atmosphere are regarded as the singular point of the polarization field, and the correction coefficient of the singular point is introduced, thereby constructing a high-robust skylight polarization model. And the heading is solved by minimizing the objective function related to AOP. On this basis, the theoretical AOP is further constructed by the proposed model, and the polarization sensor model is used as the mapping function between the theoretical AOP and the measured AOP, and then realize the outdoor field calibration, which separates the sensor error from the sky polarization model error and reduces the calibration cost and simplifying the calibration process. Finally, the actual rooftop experiment is carried out to verify that the field calibration based on the improved Berry model can reduce the average STD of heading error by 20.86% compared with that of the Berry model and 92.85% compared with that of the Rayleigh model with changing solar altitude. The results show that the skylight polarization model considering depolarization is very effective in improving the robustness and accuracy of heading measurement. Future research work will focus on improving the optical path structure to obtain more accurate AOP values and studying algorithms such as image denoising and anti-occlusion to make it adapt to complex environments.

REFERENCES

[1] Z. Wan, K. Zhao, and J. Chu, "Robust azimuth measurement method based on polarimetric imaging for bionic polarization navigation," *IEEE Trans. Instrum. Meas.*, vol. 69, no. 8, pp. 5684–5692, Aug. 2020.

[2] J. Yang, T. Du, X. Liu, B. Niu, and L. Guo, "Method and implementation of a bioinspired polarization-based attitude and heading reference system by integration of polarization compass and inertial sensors," *IEEE Trans. Ind. Electron.*, vol. 67, no. 11, pp. 9802–9812, Nov. 2020.

[3] J. Yang, X. Liu, Q. Zhang, T. Du, and L. Guo, "Global autonomous positioning in GNSS-challenged environments: A bioinspired strategy by polarization pattern," *IEEE Trans. Ind. Electron.*, vol. 68, no. 7, pp. 6308–6317, Jul. 2021.

[4] S. B. Powell, R. Garnett, J. Marshall, C. Rizk, and V. Gruev, "Bioinspired polarization vision enables underwater geolocalization," *Sci. Adv.*, vol. 4, no. 4, Apr. 2018, Art. no. eaao6841.

[5] J. Dupeyroux, J. R. Serres, and S. Viollet, "AntBot: A six-legged walking robot able to home like desert ants in outdoor environments," *Sci. Robot.*, vol. 4, no. 27, p. 12, Feb. 2019.

[6] J. Dupeyroux, J. Diperi, M. Boyron, S. Viollet, and J. Serres, "A bio-inspired celestial compass applied to an ant-inspired robot for autonomous navigation," in *Proc. Eur. Conf. Mobile Robots (ECMR)*, New York, NY, USA, Sep. 2017, pp. 1–6.

[7] J. Zhang, J. Yang, S. P. Wang, X. Liu, Y. Wang, and X. Yu, "A self-contained interactive iteration positioning and orientation coupled navigation method based on skylight polarization," *Control Eng. Pract.*, vol. 111, p. 11, Jun. 2021.

[8] R. B. Lindsay, *On Light From Sky, Its Polarization Colour (1871)*. New York, NY, USA: Pergamon, 1970, pp. 85–92.

[9] H. Jin, X. Wang, Z. Fan, and N. Pan, "Linear solution method of solar position for polarized light navigation," *IEEE Sensors J.*, vol. 21, no. 13, pp. 15042–15052, Jul. 2021.

[10] W. Sturzl and N. Carey, "A fisheye camera system for polarisation detection on UAVs," in *Proc. 12th Eur. Conf. Comput. Vis. (ECCV)*, in Lecture Notes in Computer Science, vol. 7584. Berlin, Germany: Springer-Verlag, 2012, pp. 431–440.

[11] W. Sturzl, "A lightweight single-camera polarization compass with covariance estimation," in *Proc. IEEE Int. Conf. Comput. Vis. (ICCV)*, New York, NY, USA, Oct. 2017, pp. 5363–5371.

[12] J. Tang et al., "Application of polarized light compass system on solar position calculation," *Optik*, vol. 187, pp. 135–147, Jun. 2019.

[13] Y. Fan, R. Zhang, Z. Liu, and J. Chu, "A skylight orientation sensor based on S-Waveplate and linear polarizer for autonomous navigation," *IEEE Sensors J.*, vol. 21, no. 20, pp. 23551–23557, Oct. 2021.

[14] H. J. Liang, H. Y. Bai, N. Liu, and X. B. Sui, "Polarized skylight compass based on a soft-margin support vector machine working in cloudy conditions," *Appl. Opt.*, vol. 59, no. 5, pp. 1271–1279, 2020.

[15] W. Zhang, Y. Cao, X. Zhang, Y. Yang, and Y. Ning, "Angle of sky light polarization derived from digital images of the sky under various conditions," *Appl. Opt.*, vol. 56, no. 3, pp. 587–595, Jan. 2017.

[16] M. Hamaoui, "Polarized skylight navigation," *Appl. Opt.*, vol. 56, no. 3, pp. B37–B46, 2017.

[17] J. Liu et al., "Attitude calculation method based on full-sky atmospheric polarization mode," *Rev. Sci. Instrum.*, vol. 90, no. 1, Jan. 2019, Art. no. 015009.

[18] B. Mayer, "Radiative transfer in the cloudy atmosphere," in *Proc. EPJ Web Conf.*, vol. 1, 2009, pp. 75–99.

[19] H. Cheng, J. Chu, R. Zhang, L. Tian, and X. Gui, "Turbid underwater polarization patterns considering multiple Mie scattering of suspended particles," *Photogramm. Eng. Remote Sens.*, vol. 86, no. 12, pp. 737–743, Dec. 2020.

[20] H. Cheng, J. Chu, R. Zhang, and P. Zhang, "Simulation and measurement of the effect of various factors on underwater polarization patterns," *Optik*, vol. 237, Jul. 2021, Art. no. 166637.

[21] L. H. Wu, J. Zhang, Z. G. Fan, and J. Gao, "An analytical model for skylight polarization pattern with multiple scattering," *Acta Phys. Sinica*, vol. 63, no. 11, 2014, Art. no. 114201.

[22] M. V. Berry, M. R. Dennis, and R. L. Lee, "Polarization singularities in the clear sky," *J. Phys.*, vol. 6, p. 14, Nov. 2004.

[23] T. Yang et al., "A universal method to improve the consistency between simulated results of celestial distribution of polarized light from analytical models and measured data," *Opt. Commun.*, vol. 485, Apr. 2021, Art. no. 126696.

[24] G. L. Han et al., "Design and calibration of a novel bio-inspired pixelated polarized light compass," *Sensors*, vol. 17, no. 11, p. 17, 2017.

[25] J. Yang, T. Du, B. Niu, C. Li, J. Qian, and L. Guo, "A bionic polarization navigation sensor based on polarizing beam splitter," *IEEE Access*, vol. 6, pp. 11472–11481, 2018.

[26] X. Liu, J. Yang, L. Guo, X. Yu, and S. P. Wang, "Design and calibration model of a bioinspired attitude and heading reference system based on compound eye polarization compass," *Bioinspiration Biomimetics*, vol. 16, no. 1, p. 18, 2021.

[27] H. N. Ren, J. Yang, X. Liu, P. P. Huang, and L. Guo, "Sensor modeling and calibration method based on extinction ratio error for camera-based polarization navigation sensor," *Sensors*, vol. 20, no. 13, p. 18, 2020.

[28] Z. H. Wan, K. C. Zhao, Y. H. Li, and J. K. Chu, "Measurement error model of the bio-inspired polarization imaging orientation sensor," *Opt. Exp.*, vol. 30, no. 1, pp. 22–41, 2022.

[29] Z. G. Fan, X. Q. Wang, H. H. Jin, C. Wang, N. Pan, and D. Hua, "Neutral point detection using the AOP of polarized skylight patterns," *Opt. Exp.*, vol. 29, no. 4, pp. 5665–5676, 2021.

[30] Z. Zhang, "A flexible new technique for camera calibration," *IEEE Trans. Pattern Anal. Mach. Intell.*, vol. 22, no. 11, pp. 1330–1334, Nov. 2000.

[31] L. M. Eshelman and J. A. Shaw, "Visualization of all-sky polarization images referenced in the instrument, scattering, and solar principal planes," *Opt. Eng.*, vol. 58, no. 8, p. 1, May 2019.

[32] H. Y. Ding and Z.-F. Bian, "A sub-pixel registration approach based on Powell algorithm," *Acta Photonica Sinica*, vol. 38, no. 12, pp. 3322–3327, 2009.

[33] M. V. Rohr, "Geometrical investigation of the formation of images in optical instruments," *Chest*, 1998.

Guangmin Li was born in 1997. He received the master's degree from the Harbin Institute of Technology, Harbin, Heilongjiang, China, in 2021, where he is currently pursuing the Ph.D. degree with the School of Instrumentation Science and Engineering.

His current research interests include polarization navigation and integrated navigation technology.

Ya Zhang (Member, IEEE) was born in 1987. She received the B.S. and Ph.D. degrees from the Department of Automation, Harbin Engineering University, Harbin, China, in 2010 and 2015, respectively.

She is currently an Associate Professor with the School of Instrumentation Science and Engineering, Harbin Institute of Technology, Harbin. Her current research interests include bionic polarization navigation and high-precision inertial measurement technology.

Shiwei Fan was born in 1993. He received the Ph.D. degree from the Harbin Institute of Technology, Harbin, Heilongjiang, China, in 2020.

He holds a post-doctoral position at the School of Instrumentation Science and Engineering, Harbin Institute of Technology. His current research interests include inertial navigation systems and cooperative navigation systems.

Yanyan Wang was born in 1992. She received the B.S. degree from Harbin Engineering University, Harbin, China, in 2016. She is currently pursuing the Ph.D. degree with the School of Instrumentation Science and Engineering, Harbin Institute of Technology, Harbin.

Her current research interests include deformation measurement, integrated navigation, and transfer alignment navigation systems.

Fei Yu received the B.S. degree from the Dalian University of Technology, Dalian, China, in 1997, and the M.Eng. and Ph.D. degrees from Harbin Engineering University, Harbin, China, in 2003 and 2005, respectively.

He is currently a Professor with the School of Instrumentation Science and Engineering, Harbin Institute of Technology, Harbin. His current research interests include inertial navigation systems.